AEDC-TR-76-84

$c_1\ 3$

A DIRECT COMPARISON OF ANALYTICAL AND EXPERIMENTAL SURFACE AND FLOW-FIELD DATA ON A 4-DEG CONE AT INCIDENCE IN A HYPERSONIC STREAM WITH LAMINAR BOUNDARY LAYERS

VON KÁRMÁN GAS DYNAMICS FACILITY
ARNOLD ENGINEERING DEVELOPMENT CENTER
AIR FORCE SYSTEMS COMMAND
ARNOLD AIR FORCE STATION, TENNESSEE 37389

August 1976

Final Report for Period June 5 — July 2, 1975

Approved for public release; distribution unlimited.

Prope...

F40600-76-C 0001

This report has been reviewed by the Information Office (OI) and is releasable to the National Technical Information Service (NTIS). At NTIS, it will be available to the general public, including foreign nations.

APPROVAL STATEMENT

This technical report has been reviewed and is approved for publication.

FOR THE COMMANDER

KEITH L. KUSHMAN
Captain, USAF
Analysis and Evaluation
    Division
Directorate of Test

ALAN L. DEVEREAUX
Colonel, USAF
Director of Test

REPORT DOCUMENTATION PAGE		READ INSTRUCTIONS BEFORE COMPLETING FORM
1. REPORT NUMBER AEDC-TR-76-84	2. GOVT ACCESSION NO.	3. RECIPIENT'S CATALOG NUMBER
4. TITLE (and Subtitle) A DIRECT COMPARISON OF ANALYTICAL AND EXPERIMENTAL SURFACE AND FLOW-FIELD DATA ON A 4-DEG CONE AT INCIDENCE IN A HYPERSONIC STREAM WITH LAMINAR BOUNDARY LAYERS		5. TYPE OF REPORT & PERIOD COVERED Final Report – June 5 – July 2, 1975
		6. PERFORMING ORG. REPORT NUMBER
7. AUTHOR(s) D. E. Boylan, W. T. Strike, and F. L. Shope, ARO, Inc.		8. CONTRACT OR GRANT NUMBER(s)
9. PERFORMING ORGANIZATION NAME AND ADDRESS Arnold Engineering Development Center (XO) Air Force Systems Command Arnold Air Force Station, Tennessee 37389		10. PROGRAM ELEMENT, PROJECT, TASK AREA & WORK UNIT NUMBERS Program Element 63311F System 627A
11. CONTROLLING OFFICE NAME AND ADDRESS Arnold Engineering Development Center (DYFS) Arnold Air Force Station, Tennessee 37389		12. REPORT DATE August 1976
		13. NUMBER OF PAGES 36
14. MONITORING AGENCY NAME & ADDRESS(if different from Controlling Office)		15. SECURITY CLASS. (of this report) UNCLASSIFIED
		15a. DECLASSIFICATION DOWNGRADING SCHEDULE N/A

16. DISTRIBUTION STATEMENT (of this Report)

Approved for public release; distribution unlimited.

17. DISTRIBUTION STATEMENT (of the abstract entered in Block 20, if different from Report)

18. SUPPLEMENTARY NOTES

Available in DDC

19. KEY WORDS (Continue on reverse side if necessary and identify by block number)

wind tunnel	pressures (surface)
tests	angles of attack
conical bodies	coder
flow (lee side)	computer programs

20. ABSTRACT (Continue on reverse side if necessary and identify by block number)

A wind tunnel investigation was conducted in the AEDC Hypersonic Wind Tunnel (C) at Mach numbers near 10 using a 4-deg half-angle cone to study lee side flow-field properties and surface pressures at angles of attack up to about 10 deg. The objective of the study was to provide data to aid in the development of a three-dimensional, hypersonic, viscous shock layer computer code capable of accurately predicting the

DD FORM 1 JAN 73 1473 EDITION OF 1 NOV 65 IS OBSOLETE

20. ABSTRACT (Continued)

static stability characteristics of slender bodies at incidence.
The results of the present investigation indicate that additional
development of the computer code in question is required to
fulfill this objective.

AFSC
Arn Id AFS Tenn

PREFACE

CONTENTS

ILLUSTRATIONS

TABLE

1.0 INTRODUCTION

Hypersonic viscous effects on reentry vehicle static stability have become increasingly important with the advent of maneuvering vehicles with critically small static margins. Efforts are currently underway within the AEDC von Kármán Gas Dynamics Facility (VKF) to develop experimental and analytical techniques (Refs. 1 and 2) to study this problem. Special emphasis is being placed on development and extension of the Lubard-Helliwell three-dimensional Hypersonic Viscous Shock Layer (HVSL) code* (Ref. 3). In order to provide an experimental basis of comparison, data were obtained in the VKF Hypersonic Wind Tunnel (C) at a nominal Mach number of 10 and at free-stream Reynolds numbers varying from 0.39 to 1.85 million per foot on a sharp and slightly blunted 4-deg cone. The data obtained included surface pressures and lee side flow-field pressure and total-temperature measurements. This report describes these measurements, compares the results to analytical methods, and recommends future development.

This report is another in a series that will address the problem of ablation and viscous effects on the force and moment characteristics of slender cones. A report by Griffith, Strike, and Majors (Ref. 4) describes an experiment which studied ablation and viscous effects using very sensitive force balances and ablating models. The experimental data described in Ref. 1 was the initial report in this series and is limited to the study of static forces of sharp 4- and 5-deg cones at incidence using balance measurements under Mach 8 and Mach 10 hypersonic wind tunnel conditions.

2.0 APPARATUS AND PROCEDURE

2.1 WIND TUNNEL

Tunnel C is a closed-circuit, hypersonic wind tunnel with a 50-in.-diam test section and an axisymmetric contoured nozzle which provides a nominal Mach number of 10 over a range of pressure levels from 175 to 2,000 psia. Stagnation temperatures sufficient to avoid air liquefaction in the test section (up to 2,000°R) are maintained at all conditions. The tunnel is equipped with a model injection system, which allows removal of the model from the test section while the tunnel is in operation.

2.2 MODEL

A 4-deg half-angle stainless steel cone with an axial length of 17.876 in. and a base diameter of 2.500 in. was designed and fabricated for these experiments. The model had

---

*Referred to herein as the Lubard-Helliwell HVSL code.

three interchangeable steel noses which varied from a sharp to a blunt nose with a nose-to-model-base-radius (R_N/R_B) ratio of 0.225.

The locations of 34 model surface pressure taps and the four base pressure taps are shown schematically in Fig. 1. The model was also instrumented with four Chromel®-Alumel® thermocouples to record the model wall temperature at the stations shown in Fig. 1 by the solid symbols. The base region of this model was sealed to prevent airflow through the model support into its base region.
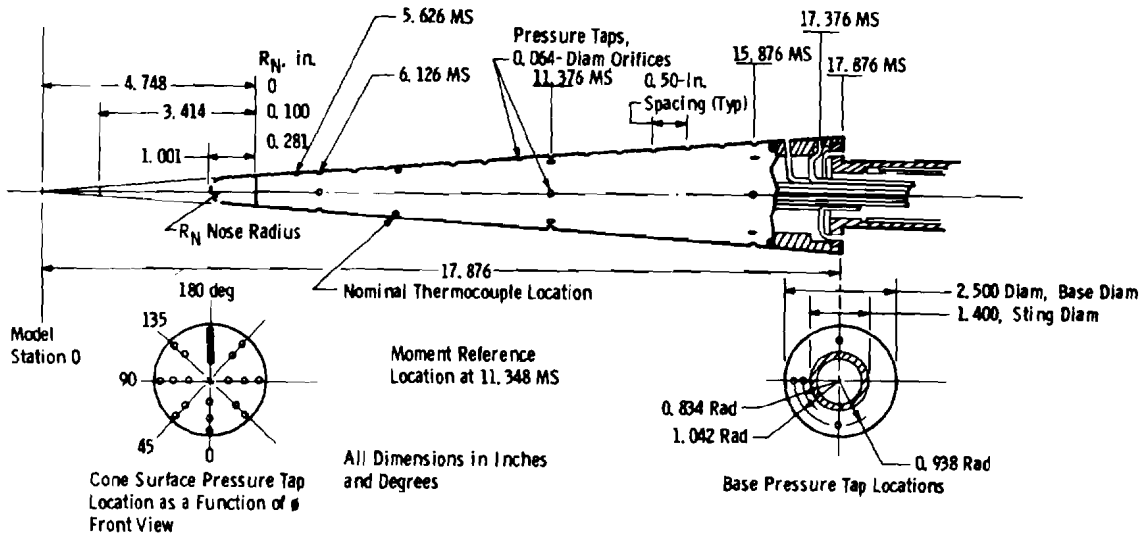
Figure 1. Four-degree half-angle cone model.

The model installation in Tunnel C is shown in Fig. 2. The ratio of the model base diameter to sting diameter was 1.786. The model sting was water cooled and tapered from a diameter of 1.400 in. at the model base to 1.955 in. at the sector adapter. The overall length of this tapered sting was nominally 9.8 model base diameters.

2.3 FLOW-FIELD RAKE AND PROBING PROCEDURE

The overhead flow-field probing mechanism shown in Fig. 2 was used to support a rake consisting of a total-temperature probe (a shielded Chromel-Alumel thermocouple) and a pitot probe. The tip of the pitot probe was flattened to an external height of 0.007 in. and a width of 0.035 in. as shown in Fig. 3. The critical dimensions of the single-shielded total-temperature probe are included in Fig. 3c.

The flow-field probing mechanism was pitched so that the probe surveys were made normal to the model axis. The limits of travel and the overall uncertainty in these movements are as follows:

Component	Survey Probe Mechanism Maximum Travel	Absolute Uncertainty
Axial, x'	38.5 in.	±0.02 in.
Lateral, y'	±9.0 in.	±0.02 in.
Vertical, z'		
Course travel	7.0 in.	±0.10 in.
Fine travel	4.0 in.	±0.003 in.
Pitch, a_p	35 deg	±0.35 deg
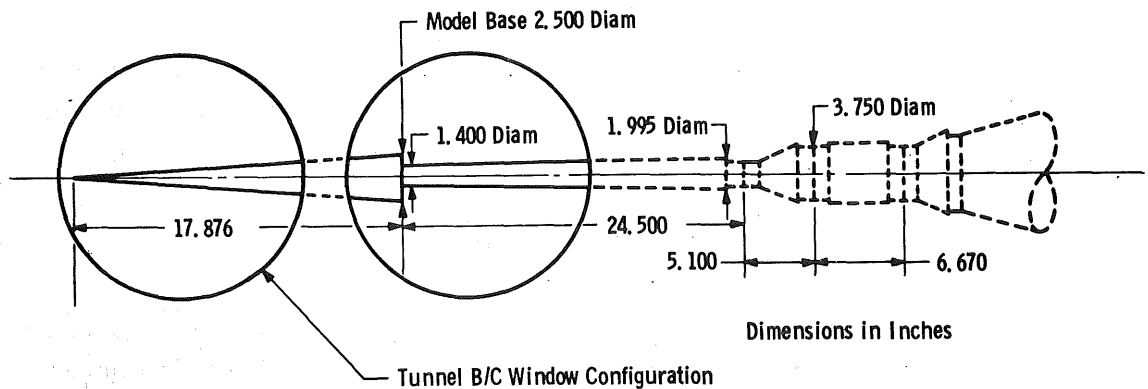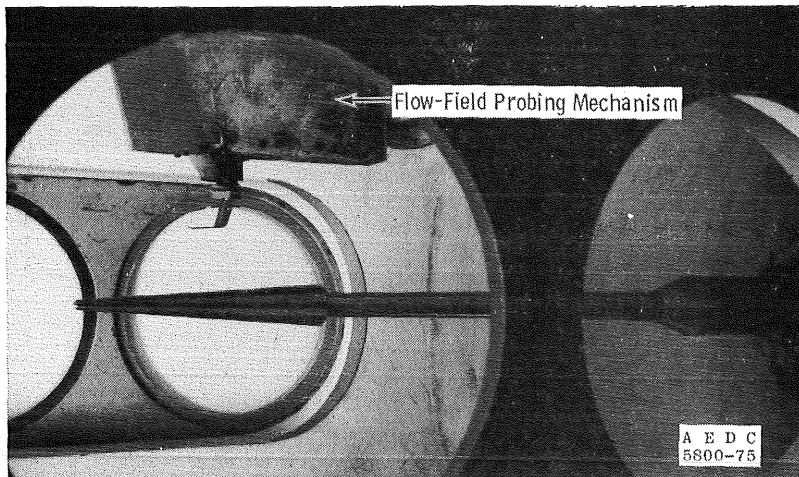
Figure 2. Model installation.

All flow-field surveys were made vertically using the "fine" travel translational capabilities of the probing mechanism. The zero position in the axial direction (x') was defined by aligning the pitot probe tip with the model base. In the lateral direction (y'), the zero position was defined when the pitot probe was directly above the row of static pressure

7

Single
Shielded
Total-
Temperature
Probe
0.056-in. ID

0.06-in.-
diam Wall
Static Taps
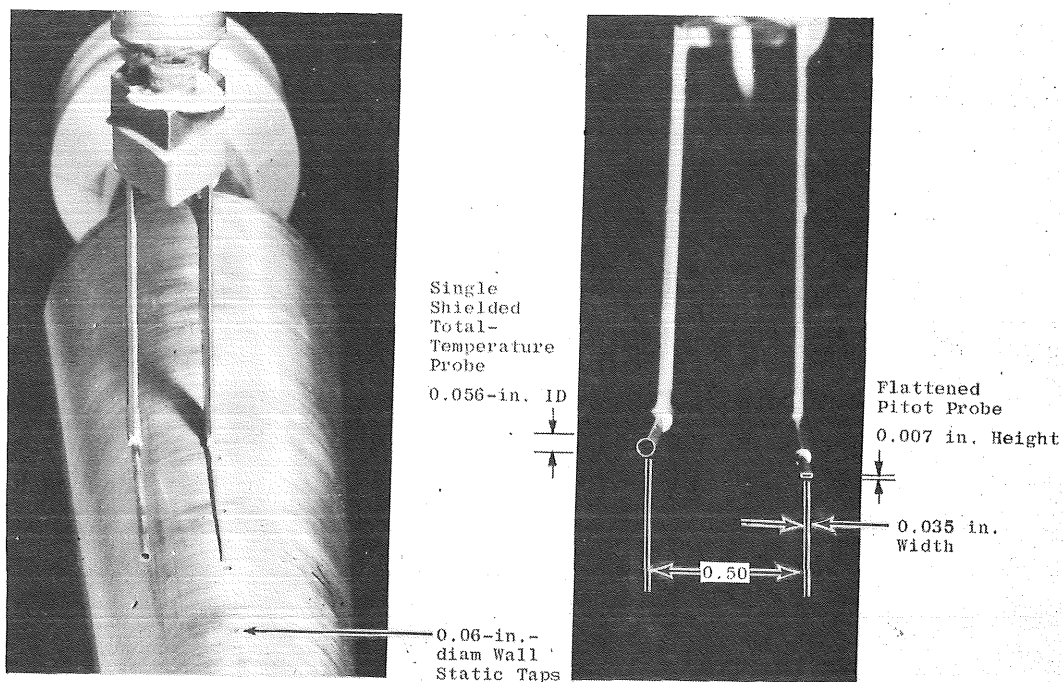
a. Flow-field survey rake
and model

Flattened
Pitot Probe
0.007 in. Height

0.035 in.
Width

0.50

b. Rake geometry

Total Temperature Probe

0.060 OD

0.056 ID

Exposed Wire

Lava
Cement

0.112

0.668

4 Vent Holes
0.020 Diam
(Displaced Axially
0.063 in.)

All Dimensions
in Inches

0.50

1.50
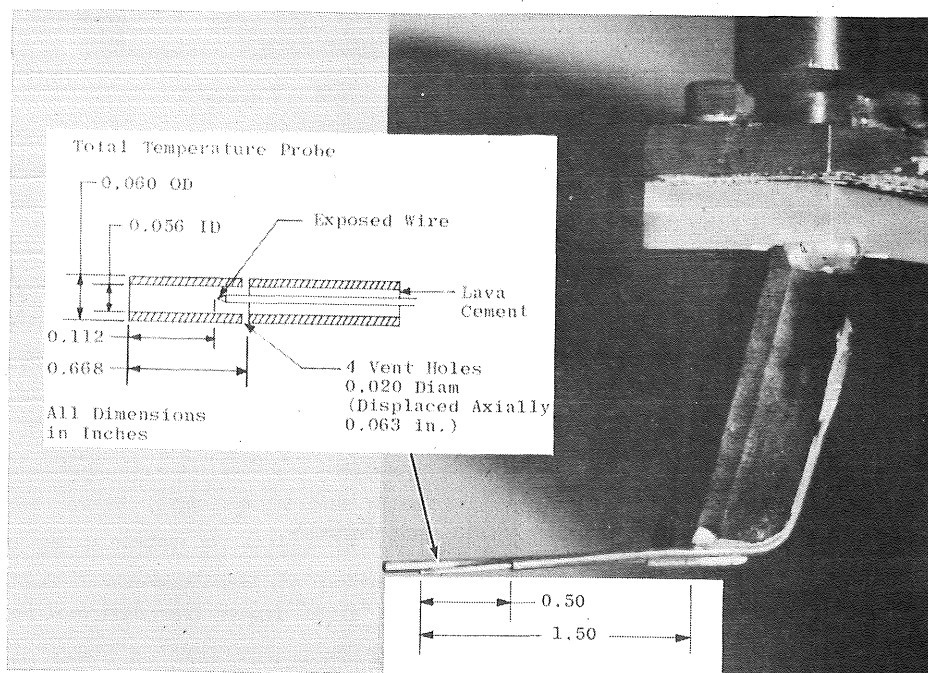
c. Profile of dual probe rake

Figure 3. Flow-field survey rake.

taps on the model surface with the model in the zero roll position as shown in Fig. 3a. The vertical zero ($z' = 0$) position was defined when the pitot probe was in contact with the model surface. The flow-field probes were installed on the rake and electrically isolated from the probe support system. An electrical fouling circuit was utilized to indicate when the probe was in contact with the model surface.

All the flow-field results are presented in the coordinate system of the Lubard-Helliwell HVSL analysis. The coordinate transformation from the coordinates of the probing mechanism to the HVSL analysis is shown in Fig. 4. Therefore, the data are presented in a coordinate system which is normal to the cone surface normalized by the slant (surface) length (ℓ_s) of the cone.
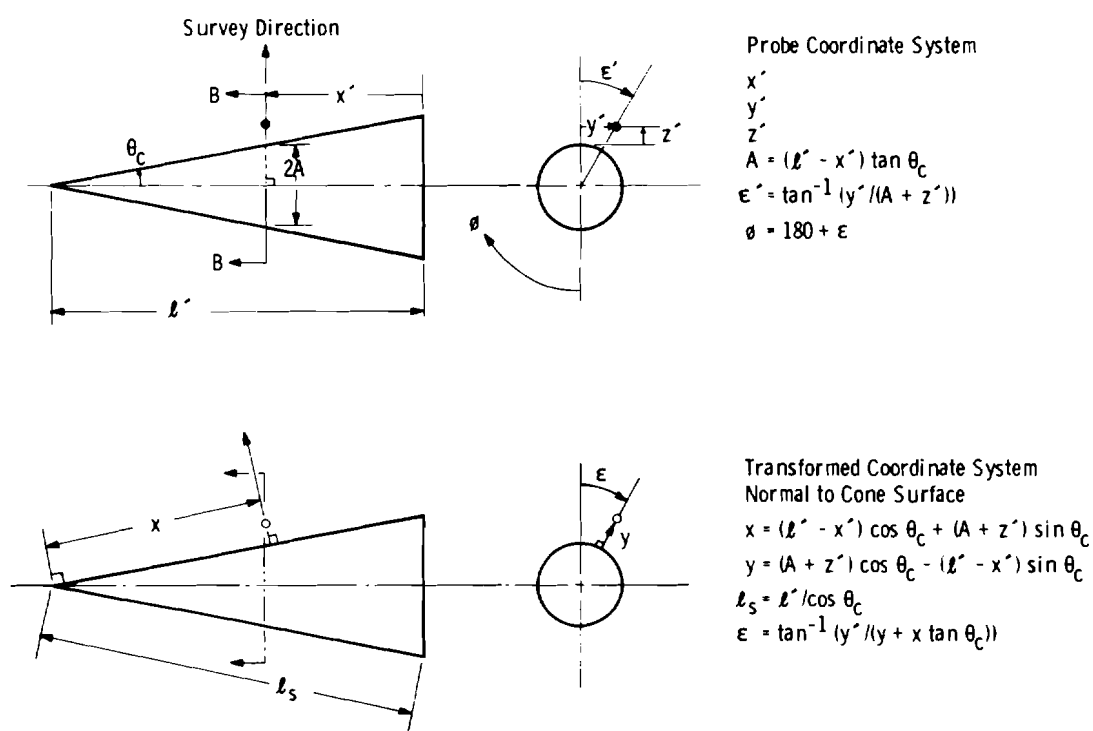
Figure 4. Coordinate systems for flow-field surveys.

2.4 TEST PROGRAM

The experimental data were obtained at the following Tunnel C test conditions:

M_∞	p_o, psia	T_o, °R	Re_∞/ft × 10^{-6}	p_∞, psia	T_∞, °R
10.10	1,500	1,900	1.85	0.0322	93
10.00	990		1.23	0.0224	95
10.00	900		1.12	0.0204	95
9.82	300		0.39	0.0076	98

9

The test matrix included surface pressure measurements as a function of model angle of attack and roll angle and also flow-field surveys consisting of pitot pressure and total-temperature distributions above the lee side ray of the model. The flow-field surveys were made normal to the cone axis and laterally at a fixed distance above the cone axis. A summary of the test program is included in Table 1.

Table 1. Test Summary

4-deg Sharp Nose Cone

$R_N = 0$

Lee Side Flow-Field Data

P_o, psia	α, deg	Surface Pressure Distribution, $\phi = 0$	Surface Pressure Distribution, ϕ, varied	Vertical Survey*, Axial (x) Position, 2.0	Vertical Survey*, Axial (x) Position, 6.5	Vertical Survey*, Axial (x) Position, 11.7	Lateral Survey, z Position, x = 2.0	Lateral Survey, z Position, x = 6.5
1,500	-0.1	x						
	0.2	x						
	1.4	x						
	2.3	x						
	3.3	x						
990	0	x						
	±1.0	x						
	±2.0	x						
300	-10.0		x					
	0	x	x					
	1.1		x					
	2.0		x					
	3.0	x	x	P,T			0.47	
	3.5		x					
	7.0	x						
	10.0		x	P,T	P	P	1.0	

4-deg Blunt Nose Cone

$R_N = 0.10$ in.

| 990 | 3.0 | | x | P,T | | | 0.5 | |
| | 10.0 | | x | P,T | | | 0.5, 1.0 | |

$R_N = 0.281$ in.

300	-0.1	x						
	3.0	x	x	P,T	P,T	P	0.5	0.46
	10.0		x	P,T			0.51, 1.0	

*P, pitot probe on model centerline.
 T, total-temperature probe on centerline.

This report presents a relatively small percentage of the data generated with this test matrix; the remainder of the data will serve as a data bank for future analysis.

The initial test runs (made at the maximum tunnel stagnation pressure of 1,500 psia and at -0.1- and 0.2-deg angle of attack) data were used to aerodynamically infer the zero angle-of-attack attitude of the cone. That is, the indicated angle of attack at which the pressures on the zero and 180-deg ray of the cone were equal was defined as zero angle of attack. This zero angle-of-attack position was then confirmed by optical means.

Cone surface pressure distribution data were obtained at a constant angle of attack as the cone was rolled in increments of 10 or 30 deg. These circumferential sharp cone surface pressure distributions were then integrated to define pressure-induced normal force, pitching moment, and axial forces acting on the cone.

Vertical flow-field surveys were made at three nominal axial positions with either the pitot probe or total-temperature probe aligned laterally with the cone axis. Also, a few lateral surveys listed in Table 1 were made at fixed positions above the cone surface at fixed positions (2.0 or 6.5 in.) upstream of the model base. The z' displacement of these lateral surveys is indicated in Table 1.

2.5 INSTRUMENTATION AND DATA PRECISION

Tunnel C stilling chamber pressure was measured with a 2,500-psid transducer referenced to a near vacuum. Based on periodic comparisons with secondary standards, the uncertainty (hereafter defining a bandwidth which includes 95 percent of the residuals, the applied minus the measured value) of these transducers is estimated to be within ±0.1 percent of the calibrated pressure range. Stilling chamber temperature was measured with a Chromel-Alumel thermocouple with an uncertainty of ±7°F at 1,900°R based on the manufacturer's specifications.

These uncertainties in the basic tunnel measurements and the variations (nonuniformity) in the Mach number distribution determined from test section flow calibration were used to estimate uncertainties in other free-stream properties, using the Taylor series method of error propagation.

Test Section Conditions

Nonuniformity			Uncertainty (±), percent			
M_∞	ΔM_∞	p_o	T_o	p_∞	T_∞	Re_∞/ft
10.10	±0.02	0.2	0.4	1.3	0.5	0.7
10.00	±0.02	0.3	0.4	1.4	0.5	0.7
9.82	±0.02	0.2	0.4	1.3	0.5	0.7

Model surface pressures were measured with the standard Tunnel C pressure system consisting of 1-psid transducers with calibrated ranges of 0.065- and 0.20-psia ranges. The estimated uncertainty in these pressure measurements was ±0.3 percent of the calibrated range or ±0.0005 psi, whichever was greater. The pitot probe measurements were made with a transducer calibrated with a low range of 1 psid and a higher range of 5 psid. The uncertainty in the pitot pressure, including the uncertainty in the reference pressure,

was ± 0.0011 psi in the low range to ± 0.0031 psi in the higher pressure range. The overall estimated uncertainty in the parameters presented in this document as defined by these uncertainties in the basic pressure and temperature measurements are as follows:

Data Uncertainties ($\pm$), percent

p_o, psia	Model Surface	Flow-Field Surveys				
	p_w/p_∞	p_o',ℓ	$p_o',\ell/p_\infty$	$T_o,\ell/T_\infty$	$M\ell/M_\infty$	$U\ell/U_\infty$
1,500	1.7	0.1 to 2.2	1.3 to 2.6	0.6	0.9 to 1.5	1.3
900	2.1	0.1 to 3.7	1.4 to 4.0	0.6	1.1 to 2.2	1.9
300	4.7	0.1 to 11.0	1.3 to 11.0	0.6	2.5 to 6.2	5.2

The tabulated uncertainty in the model surface pressure ratio (p_w/p_∞) is the maximum value which occurs when the nominal pressure ratio (p_w/p_∞) is 1.5. As the magnitude of this ratio increases, the uncertainty decreases. (For example, doubling the pressure ratio at p_o = 300 psia reduced the uncertainty by a factor of nearly one-half.)

Most of the uncertainty estimates, including the uncertainty in the local Mach number ($M\ell$), were based on an assumed local stream Mach number of unity. Obviously, near the model surface the uncertainty in the flow-field parameters reaches a maximum value at the minimum tunnel stagnation pressure as shown in the preceding tabulation.

The uncertainty quoted above for local Mach numbers does not reflect possible bias errors being introduced by the failure of the local static pressure to remain constant and equal to the measured wall value throughout the viscous and inviscid region. It was necessary to make this assumption in the data reduction, and the consequences of the failure of the assumption in certain cases is discussed in Section 3.5.

The uncertainty associated with the survey probe position is based on repeated calibrations of the probe driving mechanisms and the measured displacement between the pitot probe and total-temperature probe.

Probe Position Uncertainty

Coordinate	Pitot Probe, in.	Total-Temperature Probe, in.
x'	± 0.032	± 0.032
y'	± 0.020	± 0.028
z'	± 0.003	± 0.007

Assuming $x' = 2.0$ in., $y' = 0.5$ in., and $z' =$ less than 1.0 in. the estimated uncertainty of the angular position (ϵ) of the probes was nominally less than ±0.6 deg.

The model incidence was checked optically following each model injection into the tunnel test section, and the estimated uncertainty in this parameter for this test was less than ±0.05 deg.

3.0 RESULTS AND DISCUSSION

The scope of this report is limited primarily to comparisons between the experimental data and one advanced viscous flow-field code (Refs. 2 and 3). When meaningful comparisons can be made, the theoretical results of three additional inviscid flow-field codes (Refs. 5 through 8) are compared to the data. A brief description of each of the analytic methods precedes the discussion of the results.

3.1 INVISCID CONICAL FLOW CODES

A recent investigation by Jones (Ref. 5) results in an accurate and efficient numerical integration procedure for solution of the governing partial differential equations describing the supersonic or hypersonic inviscid perfect gas flow field around a sharp cone at incidence. Basically, Jones' method uses the condition of conicity to reduce the problem to a set of elliptic nonlinear partial differential equations in two independent variables. A transformation of coordinates is used to fix the boundaries, one of which is the unknown shock wave, between which the elliptic equations are numerically solved using a relaxation procedure. The method is, in many cases, limited only by the crossflow velocity expanding from subsonic to supersonic conditions (which changes the mathematical character of the governing equations from elliptic to hyperbolic), by the entropy singularity moving too far away from the surface, or by the lee side shock approaching very close to the Mach wave. In practice, these restrictions limit the maximum allowable angle of attack to a value on the order of or slightly greater than the cone semivertex angle.

For higher angles of attack, inviscid solutions have been generated using the QUICK, BLUNT, and STEIN computer programs, as developed by Marconi, Yaeger, and Hamilton in Ref. 6, which solve the full three-dimensional inviscid equations for arbitrary geometries. Solution of the equations begins with the time-dependent blunt body solution of Moretti and Bleich (Ref. 7). This program (BLUNT) solves the transonic flow problem resulting from immersing an arbitrary blunt body (geometry model provided by QUICK, a very general geometry code with a simple, convenient input format) in a supersonic free stream and provides an all supersonic starting solution for the final program (STEIN). The STEIN code uses the numerical technique developed by Moretti, Grossman, and Marconi (Ref. 8). Using a marching, second-order finite difference method, the full three-dimensional

Euler equations are solved for regions of continuous flow. Shocks are handled explicitly via the Rankine-Hugoniot relations. For present purposes, the sharp cone solution has been obtained by applying the QUICK/BLUNT/STEIN system to a spherically blunted cone with a nose-radius-to-base-radius ratio of 1/36 and marching the solution to nearly 500 nose radii downstream until the flow became conical. The usual BLUNT solution, however, was replaced with an approximate shock-layer-type starting solution similar to that used for the fully viscous problem discussed in the next section. This method was necessary to circumvent the attendant entropy layer difficulties which occur at high angles of attack and large downstream distances.

3.2 THE LUBARD-HELLIWELL THREE-DIMENSIONAL HYPERSONIC VISCOUS SHOCK LAYER (HVSL) CODE

The most applicable and accurate analytical technique currently available for the analysis of hypersonic flow over a sharp cone at incidence is the HVSL approach by Lubard and Helliwell (Ref. 3). An approximate system of governing equations is obtained from the complete steady-state compressible Navier-Stokes equations by assuming that the viscous, streamwise derivative terms are small compared with the viscous normal and circumferential derivatives. The resulting equations are valid in both the inviscid and viscous regions including the circumferential separation zone which develops on the leeward side at the higher angles of attack (greater than approximately the cone semivertex angle). Since this set of governing partial differential equations is parabolic in the streamwise direction, a marching-type numerical solution technique is used. An implicit finite-difference treatment is applied to the normal derivatives in conjunction with Newton's method of iteration for solution of the nonlinear algebraic equations which result from differencing of the circumferential derivatives. The equations are solved between the body surface and the bow shock; boundary conditions at the shock and its resulting shape are calculated by using the Rankine-Hugoniot shock-crossing relations and a one-sided differencing of the continuity equation. A thermally and calorically perfect air model is used having a constant specific heat ratio of $\gamma = 1.40$ in conjunction with the Sutherland viscosity law and a constant laminar Prandtl number of 0.71.

It is important to note and appreciate that the present HVSL approach includes both the inviscid and viscous regions of the flow field in one composite set of equations. Hence, complicated inviscid interactions which occur under hypersonic flow conditions (such as the well-known displacement-induced pressure effect) are automatically included in the analysis without tedious matching of separate inviscid and viscous solutions as would be required using higher-order boundary-layer theory.

14

The Lubard-Helliwell HVSL code is itself applicable only to right-circular cone body geometry. However, conical frustums with arbitrary forebodies or noses can be treated using the code if the flow field at the end of the forebody can be obtained for use as initial data for computing the flow over the conical frustum. A method for calculating the shock layer over a spherical nosecap has been developed from the boundary-layer method described in Ref. 9. Results from this method have been used as initial data at the sphere-cone tangency to allow the computation of the flow over the conical portion of a spherically blunted cone using the Lubard-Helliwell HVSL code. In the method developed for the spherical nosecap region, it has been assumed that the Reynolds number is high enough that the shock layer thickness and pressure field are essentially those obtained by methods for inviscid flow, and results from the method of Ref. 10 have been used for these quantities. Results obtained by combining this method for the nose with the Lubard-Helliwell HVSL method for the conical frustum have agreed reasonably well with a variety of experimental data for laminar flow over spherically blunted cones; however, for free-stream Reynolds number based on nose radius sufficiently small (say, $Re_{\infty R_N} \leq 10,000$), an improved method for treating the nose region is needed. One comparison of blunt body data with the Lubard-Helliwell HVSL code results will be presented herein.

Adams (Ref. 2) has developed a technique whereby initial conditions for the case of sharp-cone-at-incidence flows can be generated using the same Lubard-Helliwell code for the downstream marching solution. Briefly, reasonable initial profiles and circumferential shock shapes are chosen for some location near the sharp cone apex but downstream of the merged-layer region near the cone tip. The initial shock shape can be taken from the Jones' solution for inviscid flow over sharp cones at incidence (restricted to angle-of-attack range less than approximately the cone half-angle). For larger angles of attack, the Jones' results may be extrapolated for the initial guess. Given these initial profiles, the solution is marched downstream using a very small constant Δx step size for a distance of approximately ten maximum initial viscous layer thicknesses at which time the solution appears (in all cases run to date) to reflect the parabolic nature of the governing equations and solution procedure, i.e., the effect of the initial conditions becomes less and less important as the solution marches downstream. Typically, this "adjustment" region is located within an interval of 2.5 to 8.5 percent of the cone length. With the initial conditions determined per the above-discussed method, the solution continues downstream using the Lubard-Helliwell code in conjunction with the well-known Courant-Friedrichs-Lewy criterion to determine the maximum allowable Δx step size for a given (input) circumferential $\Delta \phi$ step size. Nonuniform grid node distributions are employed in both the body normal and circumferential directions (typically 50 points in the body normal grid and 26 points in the circumferential grid); a geometric progression

scheme is used to cluster body normal points near the wall where viscous effects are dominant. The original circumferential iteration logic as given in Ref. 3 has been modified slightly to more properly reflect the elliptic character of the governing shock layer equations in the circumferential direction.

It should be noted that while the Lubard-Helliwell HVSL code utilized herein is based on the original analytical work described in Ref. 3, additional code development and production of solutions on a routine basis was the result of the effort described in Refs. 2 and 9. Current efforts are being undertaken in the development of this code which will be described in Section 3.6. The development of a production code capable of handling arbitrary nonaxisymmetric bodies including cut biconics at high incidence angles under both laminar and turbulent boundary-layer conditions is the ultimate aim of the code development program.

3.3 SURFACE PRESSURES ON SHARP AND BLUNT 4-DEG CONES AT INCIDENCE

Previous experimental results (Ref. 1) suggested that aerodynamic forces on slender bodies at angles of attack near or greater than the body half-angle are highly dependent on lee side surface conditions. The present experiment was therefore designed to accurately measure surface pressures at a sufficient number of model locations to accurately define the required pressure distributions to allow numerical integrations and arrive at pressure-induced aerodynamic forces. This procedure made it possible to compare surface pressure distributions (longitudinally and circumferentially) with the analytical results of the Lubard-Helliwell-HVSL code. Surface pressure distributions on three model rays on both a sharp and blunt 4-deg cone at angle of attack near 3 deg are shown in Figs. 5 and 6 normalized by free-stream static pressure. The error bands of 4.7, 3.6, and 2.5 percent shown in Fig. 5 reflect the computed absolute uncertainties discussed in Section 2.3. In general, the data are observed to scatter about a faired line much less than these computed uncertainties. For the case of the sharp cone data (Fig. 5), the Lubard-Helliwell-HVSL solution on the windward ray is in excellent agreement with the experimental data, while the data on the 90- and 180-deg rays (yaw and lee) fall consistently about four or five percent below the Lubard analysis. In all cases the experimental data are significantly above the sharp cone inviscid solutions (Ref. 5) which are tabulated on Fig. 5. The comparison of the blunt cone data to the Lubard analysis (Fig. 6) indicates much better agreement on both the windward and leeward surfaces. Again, the present data are at a considerably higher absolute level than the inviscid predictions.
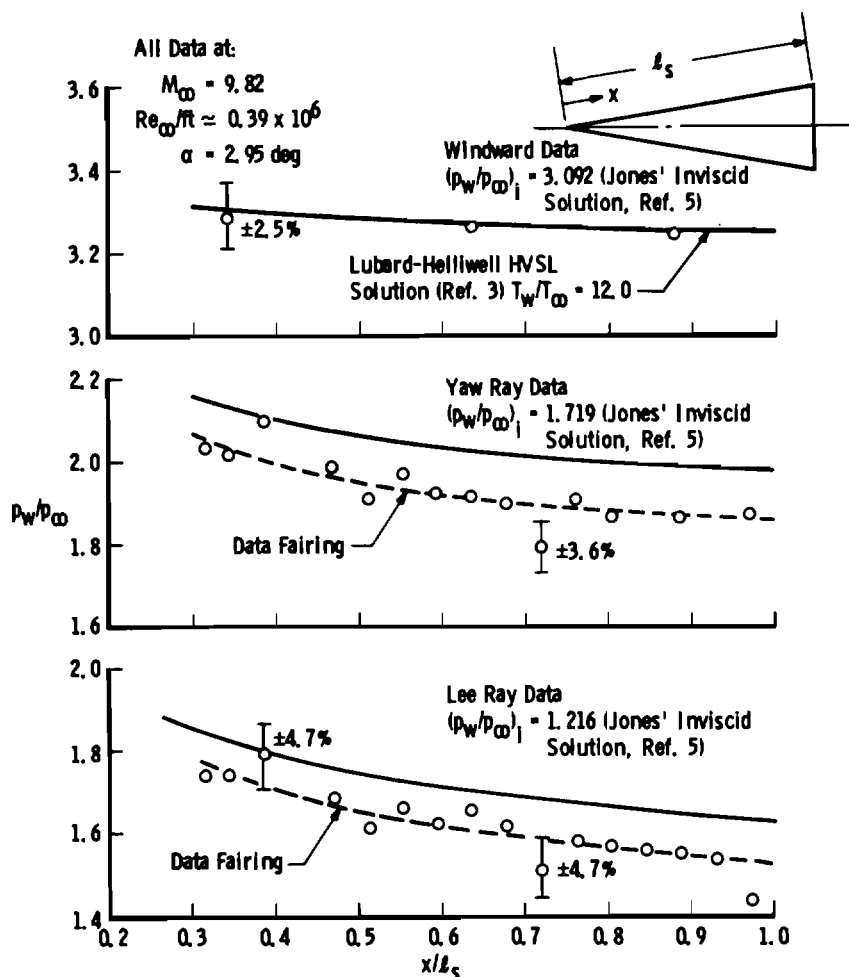
Figure 5. Wall pressure distribution on a 4-deg sharp cone at incidence.

Data on the 4-deg sharp cone at a much higher angle of attack are shown in Fig. 7. The divergence between the measured and analytical results appears to begin at 70 or 80 deg from the windward ray with the percentage difference on the model leeward side being larger near the front of the model. At the 31-percent model station and ϕ = 130 deg, the ratio of p_w/p_∞ calculated by the Lubard-Helliwell HVSL code to the measured value is about 1.5. The inviscid STEIN solution shown in Fig. 7 is consistently less than either the experiment or the viscous theory. The sharp recompression in the inviscid solution at about ϕ = 158 deg, which represents an inviscid crossflow shock, appears in neither the experimental data nor the Lubard-Helliwell HVSL solution where the recompression gradients are smeared by the viscosity. This increasing difference on the

17

model leeward ray with increasing angle of attack is shown again in Fig. 8. Good agreement on the windward surface between the Lubard-Helliwell HVSL code and experimental measurements is apparent with increasing differences on the leeward ray as model angle

All Data at:

M_∞ = 9.82

$Re_\infty/ft \simeq 0.39 \times 10^6$

α = 2.97 deg

R_N/R_B = 0.225

$T_w/T_\infty \simeq 11.0$

Sym	Model Ray
O	Wind
□	Lee

Lubard-Helliwell HVSL Solutions (Ref. 3) T_w/T_∞ = 11

Stein Inviscid Solutions (Refs. 6, 7, and 8)

Sphere-Cone Tangent Point at x/ℓ_s = 0.2245
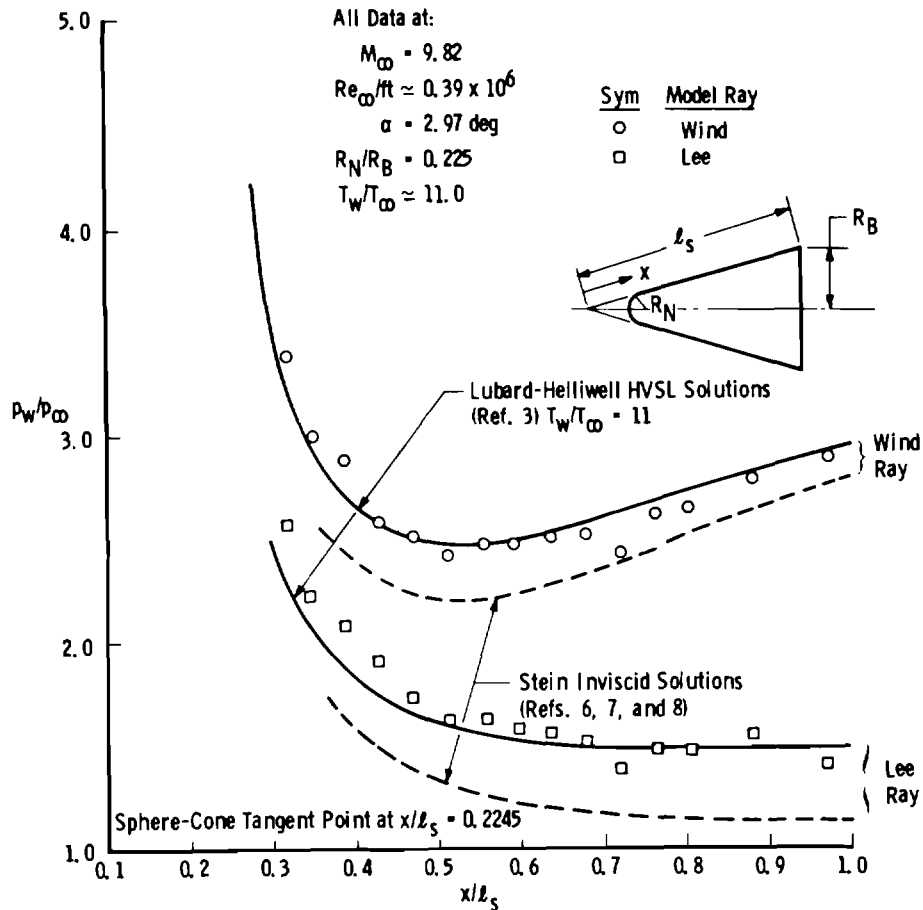
Figure 6. Wall pressure distribution on a 4-deg blunt cone at incidence.

of attack is increased. The inflection point on the leeward curve is a manifestation of a fundamental change in the nature of the flow beyond $a = \theta_c$, namely the formation of two counter-rotating vortices in the lee side flow. All data shown in Fig. 8 were obtained at the 89-percent model station.
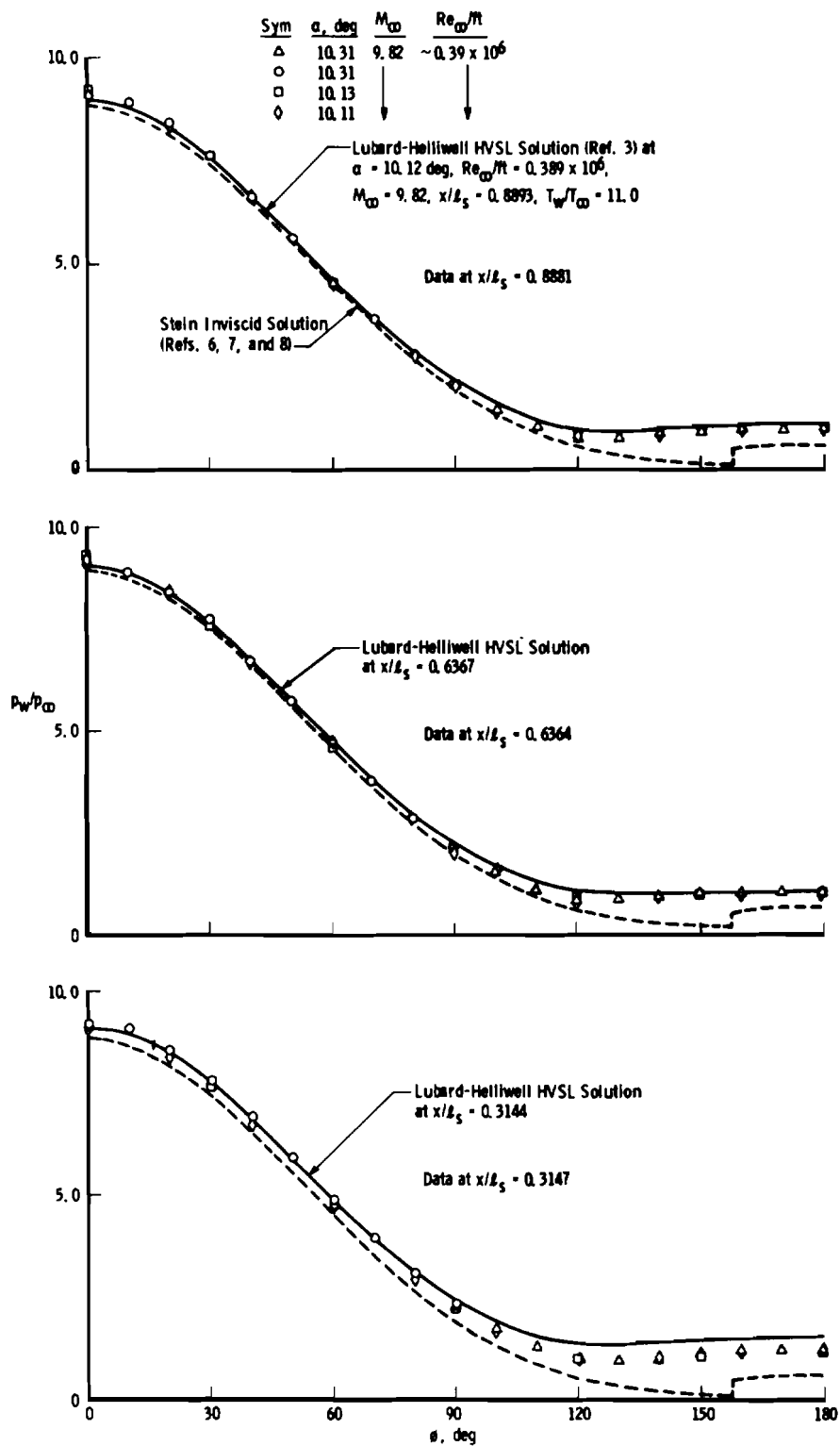
Figure 7. Circumferential surface pressures on a sharp 4-deg cone at incidence.
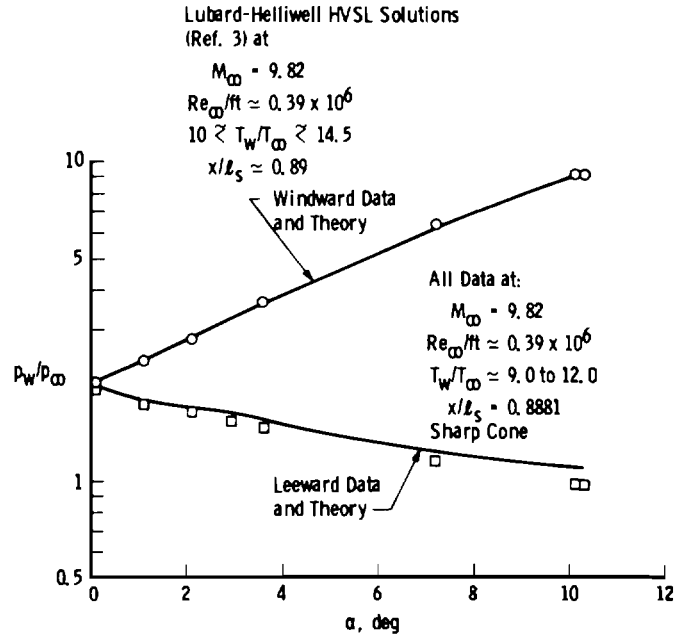
Lubard-Helliwell HVSL Solutions
(Ref. 3) at

$M_\infty = 9.82$
$Re_\infty/ft \simeq 0.39 \times 10^6$
$10 \lesssim T_w/T_\infty \lesssim 14.5$
$x/\ell_s \simeq 0.89$

Windward Data
and Theory

All Data at:

$M_\infty = 9.82$
$Re_\infty/ft \simeq 0.39 \times 10^6$
$T_w/T_\infty \simeq 9.0$ to 12.0
$x/\ell_s = 0.8881$
Sharp Cone

Leeward Data
and Theory

Figure 8. Windward and leeward surface pressures on a 4-deg sharp cone at incidence.

3.4 AERODYNAMIC FORCES FROM INTEGRATION OF SURFACE PRESSURES

Accurate determination of pressure-induced aerodynamic forces can be evaluated for any geometry for which sufficient pressure distributions have been obtained. The present sharp cone configuration yielded sufficient quality and quantity of required pressure data to perform numerical integrations.

The Lubard-Helliwell HVSL code as developed by Adams (Ref. 2) treats the base pressure as being equal to the free-stream pressure. The numerical integrations of the surface pressure distribution employed the same assumption so that direct comparison with the Lubard-Helliwell HVSL code (pressure contribution) could be made.

For a sharp cone at incidence, the pressure-induced aerodynamic forces can be expressed as

$$C_{A_p} = (2/\pi)(\ell'/R_B) \int_o^1 \frac{r}{R_B} \tan \theta_c \int_o^\pi C_p \, d\phi \, d(x/\ell') \qquad (1)$$

$$C_{N_p} = (2/\pi)(\ell'/R_B) \int_o^1 \frac{r}{R_B} \int_o^\pi C_p \cos \phi \, d\phi \, d(x/\ell') \qquad (2)$$

20

$$C_{M_p} = (1/\pi)(\ell'/R_B) \int_0^1 \left[\left(\frac{x_r}{\ell'} - \frac{x}{\ell'} \right) \frac{\ell'}{R_B} - \frac{r}{R_B} \tan\theta_c \right] \frac{r}{R_B} \int_0^\pi C_p \cos\phi \, d\phi \, d(x/\ell') \quad (3)$$

where the subscript p refers to pressure-induced forces and the parameter x_r refers to the length from the model nose to the arbitrary moment reference location.

An evaluation of the accuracy of the numerical integration, with the available pressure distributions, was made by evaluating integrations using an equal number and spacings of pressure distributions from an analytical solution for which integrations using a finer pressure distribution grid had been computed. The results indicated that the present experimentally derived aerodynamic forces are accurate to about ± 1.1 percent for C_{A_p}, ± 0.3 percent for C_{N_p}, ± 1.9 percent for C_{M_p} and ± 1.9 percent for center-of-pressure location.
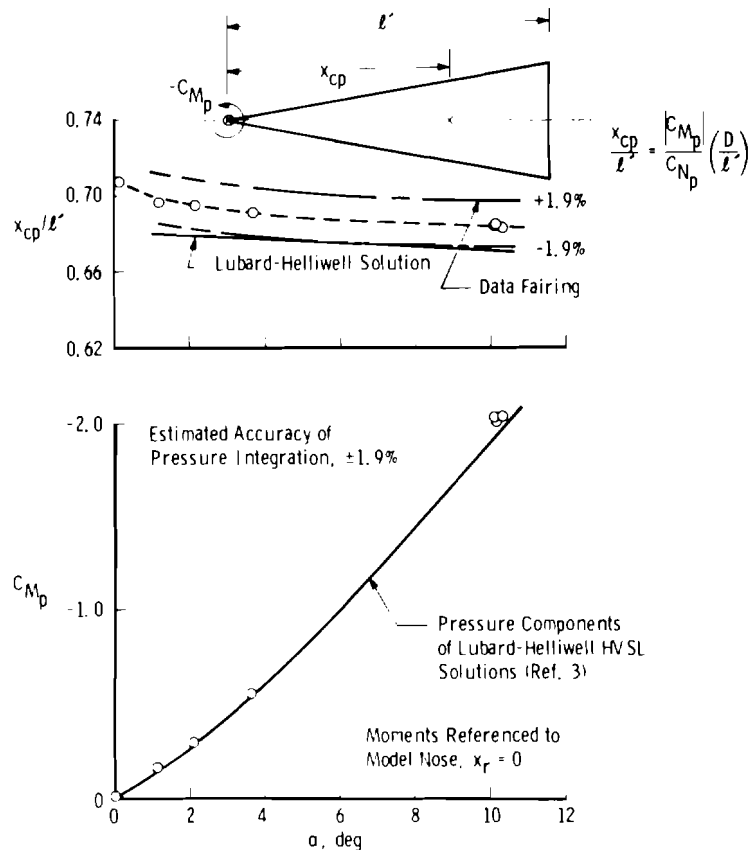
The pressure component of the Lubard-Helliwell HVSL solutions for a 4-deg sharp cone at incidence are shown compared to the present experimental data in Fig. 9. As
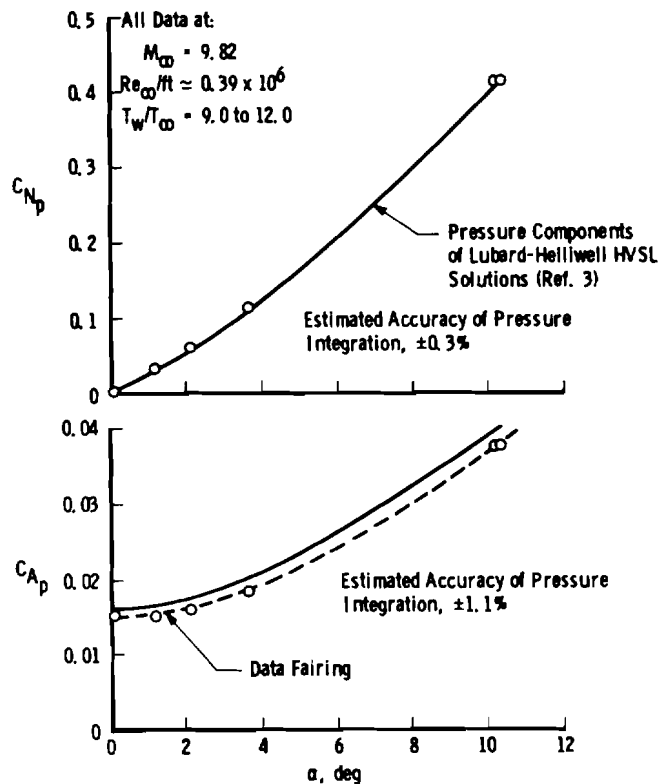
a. Axial and normal force

Figure 9. Results of sharp cone surface pressure integrations.

21

b. Static moment and center of pressure

Figure 9. Concluded.

could be expected from the integrated surface pressure data, axial forces are slightly over-predicted (five to nine percent) by the analytical code. Comparison of experimentally and analytically defined normal-force and pitching-moment coefficients are in better agreement with differences of only about three to six percent being evident at the higher incidence angles. The differences in moment and normal force are of an opposite and compensating nature resulting in similarly good agreement between predicted and measured center-of-pressure location.

It should be noted that the present aerodynamic integrated pressure force data cannot be directly compared to that presented in Ref. 4. Only pressure-induced aerodynamic forces are inferred from the present data, while in Ref. 4 balance measurements represent the combined effect of total shear and pressure forces.

3.5 LEE SIDE FLOW-FIELD STUDIES

One of the primary objectives of the test program was to obtain experimental data in the lee side flow field of a sharp and blunt slender cone at incidence. The total pressure and temperature probes described in Section 2.3 were used to obtain the required information. In a nonisentropic flow field, knowledge of total temperature and pitot pressures alone is not adequate to define all flow-field parameters. To provide the third required variable, wall pressure at the model axial station at which surveys were obtained was measured and then assumed to be constant along a normal to the surface through the viscous and inviscid flow field. Analytical solutions from the Lubard-Helliwell HVSL code indicate that on the model lee ray at small angles of attack this is a valid assumption. However, as model angle of attack and/or circumferential model ray changes, this assumption becomes less true (Fig. 10). The data contained herein are limited to cases for which this assumption is valid or the data indicate approximate corrections for the variation in local static pressure. Data obtained off the model lee ray (ϕ = 180 deg) are limited to only total-pressure and temperature profiles and do not require the static pressure assumption.

Sym	α, deg	ϕ, deg
O	2.94	180
$\triangledown$	2.94	110
$\square$	10.25	180

All Solutions at M_∞ = 9.82, T_w/T_∞ = 11.0 to 12.0, $Re_\infty/ft \simeq 0.39 \times 10^6$, $x/\ell_s \simeq 0.89$ for 4.0 deg Sharp Cone
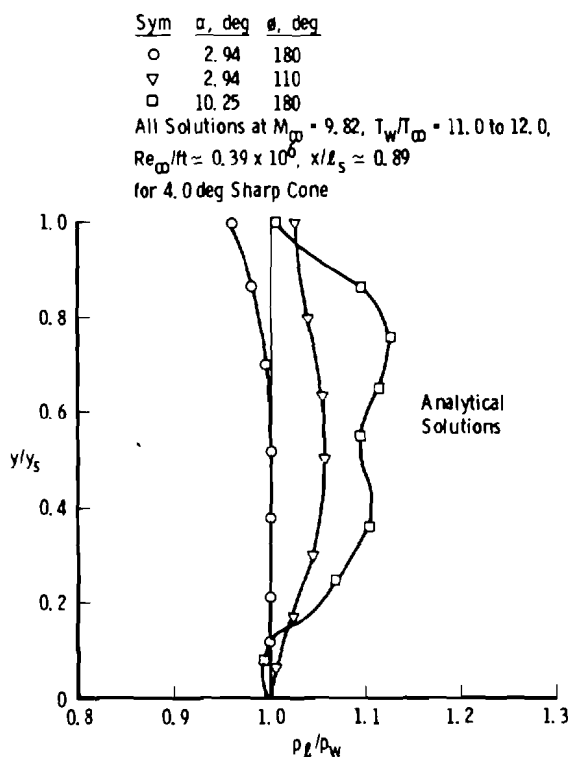
Figure 10. Analytic variation of static pressure through the flow field on a sharp 4-deg cone at incidence.

Local values of Mach number were calculated from the total and assumed static pressures by use of the perfect gas Rayleigh pitot formula

$$P_{o,\ell}'/P_\ell = \left(\frac{6M_\ell^2}{5}\right)^{3.5} \left(\frac{6}{7M_\ell^2 - 1}\right)^{2.5} \quad , \quad \gamma = 1.4 \quad (4)$$

for the supersonic portion of the boundary layer and the relationship

$$M_\ell = \sqrt{5\left((P_{o,\ell}'/P_\ell)^{0.2857} - 1\right)} \quad (5)$$

for the subsonic region of the flow field. It can be shown that a relatively large error in static pressure would be required before a significant error in local Mach number would result.

The local static temperature was calculated from the total-temperature measurements* corrected for internal probe-flow, low Reynolds number effects by the relationship.

$$T_\ell = T_{o,\ell,c}'(1 + 0.2 M_\ell^2) \quad (6)$$

The variation of local to free-stream velocities was then computed using

$$U_\ell/U_\infty = (M_\ell/M_\infty) \sqrt{T_\ell/T_\infty} \quad (7)$$

The preceding data reduction technique indicates that local total-pressure and corrected total-temperature measurements are needed at the same physical location within the flow field. This was accomplished by combining the total-temperature and pitot pressure data from two flow-field surveys and performing a 5-point Lagrangian data interpolation, correcting the total-temperature probe measurements, and another interpolation to arrive at the flow-field properties at the position of the pitot pressure probe. This procedure implicitly assumes that the positions of the probes were known to a high degree of accuracy. Unfortunately, experience indicated that this was not always the case. The resulting uncertainty in the manipulated data when combined with the uncertainty in absolute measurements, the method of total-temperature probe correction, and the use of perfect gas relationships in a real gas flow field suggests that the following comparisons of measured and inferred flow-field properties to the analytical solutions should be regarded from only a qualitative viewpoint.

---

*The correction procedure for the total-temperature measurements was developed by Dr. M. O. Varner. The magnitude of the correction was usually less than six percent of the measured value.

A total-pressure profile normal to the surface on the 4-deg sharp cone at an angle of attack of 2.94 deg is shown in Fig. 11a. Except near the wall $(y/\ell_s < 0.03)$, agreement
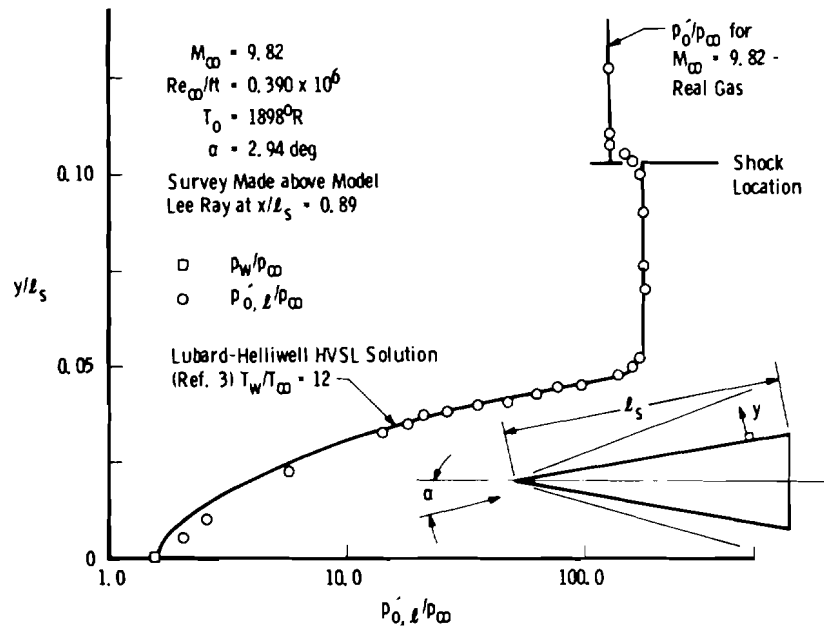
a. Total-pressure profile

Figure 11. Lee ray flow-field vertical surveys on a 4-deg sharp cone at a = 2.94 deg.
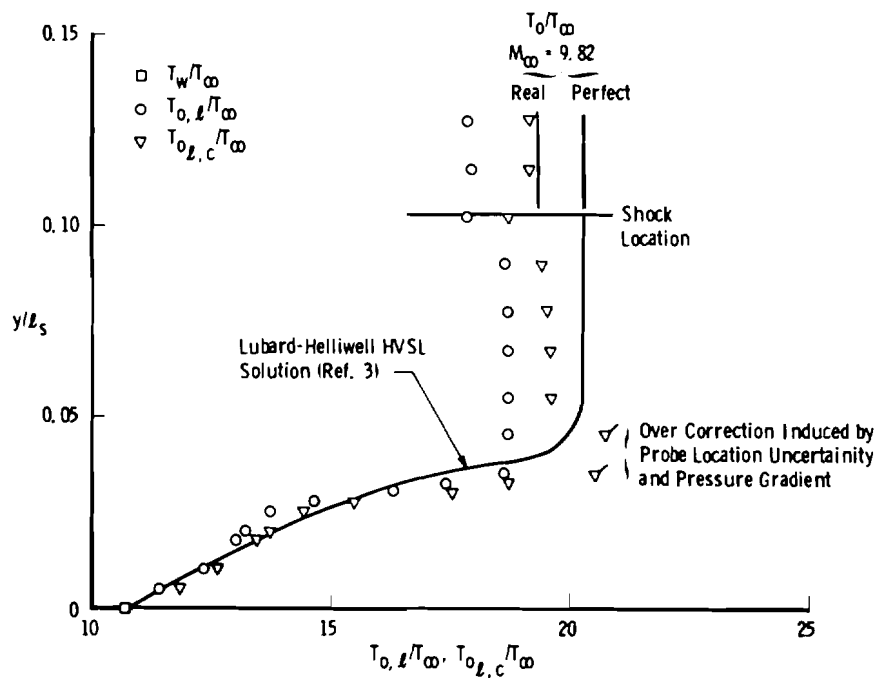
b. Total temperature

Figure 11. Continued.

25

c. Mach number and velocity
Figure 11. Concluded.

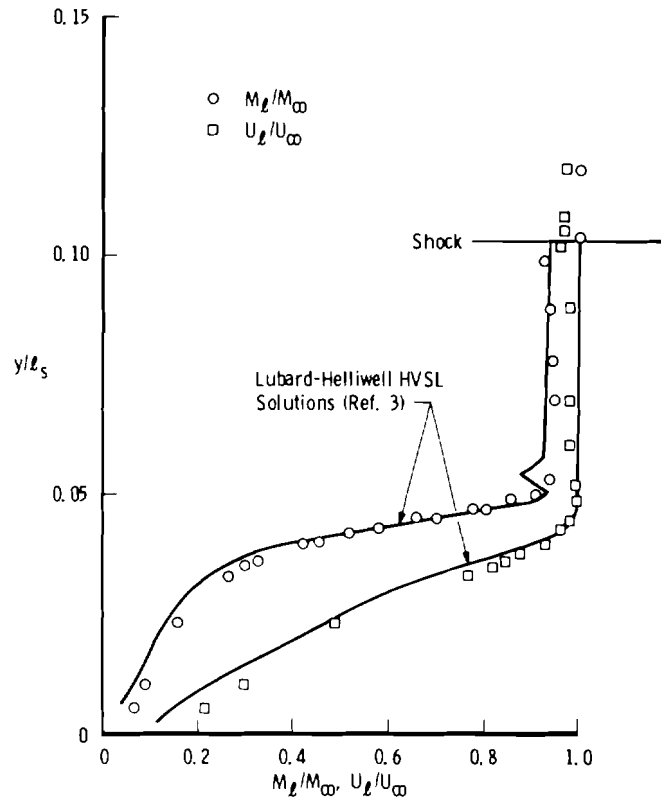between the Lubard-Helliwell HVSL code and the measured values is excellent and analytical and experimental shock locations are in good agreement. Total-temperature gradients through the flow field are shown in Fig. 11b. Both the uncorrected values of total temperature and corrected values are substantially below the Lubard-Helliwell HVSL solution in the inviscid portion of the flow field. However, this disagreement is largely due to the fact that the analytical solutions assume perfect gas relationships while the data are in a real gas flow field. The corrected values of total temperature fall within a few percent of the known real gas free-stream value. The over-correction of the total-temperature data which occurred near the "knee" of the profile is believed to be caused by a combination of small inaccuracies in probe location and the large pressure gradient at this location (Fig. 11a). Other data obtained during this study did not exhibit this characteristic and the overshoot above the inviscid level is not considered to be real. Total pressure and temperature, with measured wall pressure, are converted by Eqs. (5) through (7) to local Mach number and velocities and the results are shown in Fig. 11c. Agreement in both cases with the Lubard-Helliwell HVSL code is good.

Similar data with the model at 10.25 deg angle of attack is shown in Fig. 12. Compared with the lower incidence angle results, the comparison of experimental total pressure and
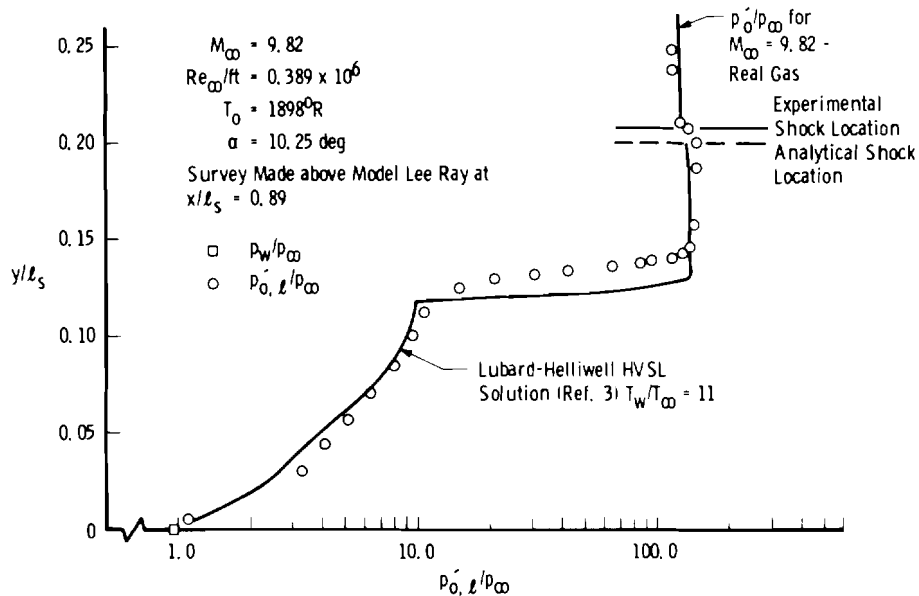
a. Total-pressure profile

Figure 12. Lee ray flow-field vertical surveys on a 4-deg sharp cone at a = 10.25 deg.
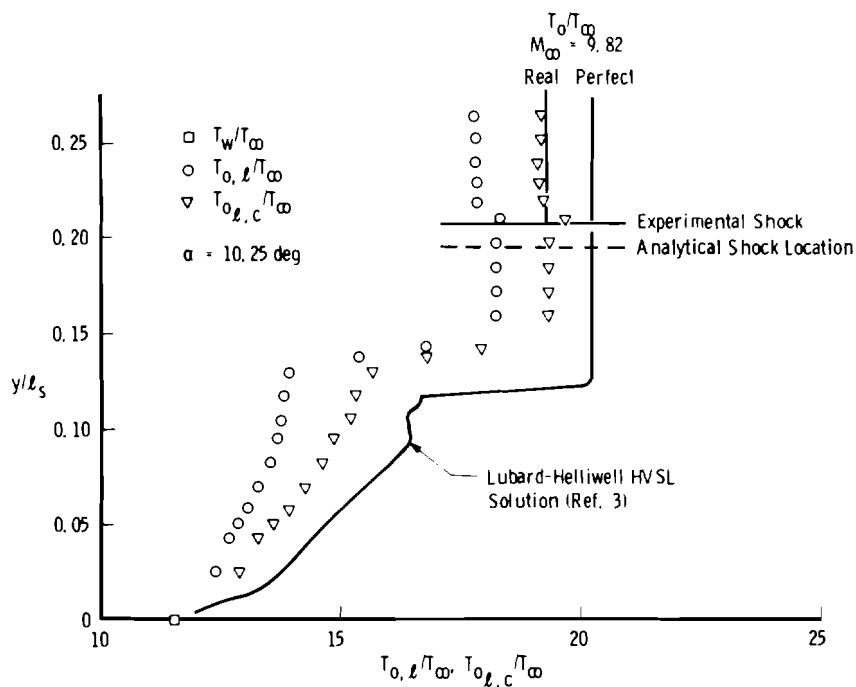
b. Total temperature

Figure 12. Continued.

27
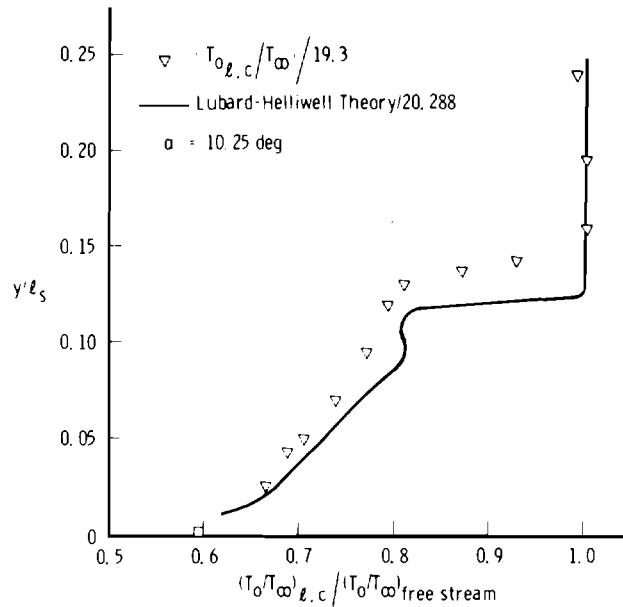
c. Total-temperature gradient
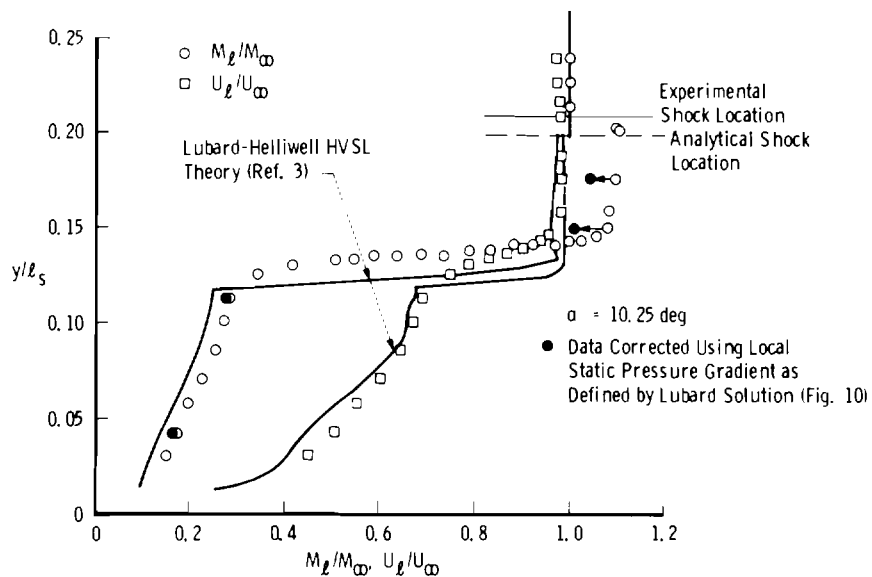
d. Mach number and velocity
Figure 12. Concluded.

temperatures with analytical results is not as good (Figs. 12a and b). The present experimental data suggest a substantially thicker viscous layer than the Lubard-Helliwell HVSL code computation indicates. Also, analytical and experimental shock location (as defined by total pressure) were different by an absolute value of about 0.14 in. which

is much greater than the probe position uncertainty of ±0.003 in. The corrected total-temperature data and the Lubard-Helliwell HVSL results were normalized by their respective free-stream values to remove the real gas effects discussed earlier. The results are shown in Fig. 12c and suggest a rather large difference between measured and calculated local total temperatures at some locations in the lee side flow field. The data, in terms of local Mach number and velocity, are shown in Fig. 12d. The assumption of constant static pressures through the flow field appears to be invalid for this condition (Fig. 10), and the effect of a static pressure gradient on several discrete data points is indicated in the data plot. Some improvement in the agreement can be seen to result between the experimental and analytical results.

It is important to note here the fundamentally different characters of the flows illustrated by Figs. 11 and 12. Whereas the total pressure and temperature profiles for the 2.94-deg angle-of-attack case are relatively smooth, the 10.25-deg case shows a sharp knee in both profiles at a height of 0.136 ℓ_s in addition to a modified shock structure and expanded region of viscous interaction. These effects are due to the two counter-rotating vortices which form under the leeward shock for $a > \theta_c$. It is a tribute to the developers of the current form of the HVSL code that such complicated flows succumb to their model and solution procedure. A further point to consider is that the total-temperature correction does not account for the gradient in the total pressure since, in fact, it is not known precisely how the vortex affects the temperature profile in the presence of severe pressure gradients. A more complete understanding of this phenomenon, along with the attendant improvements in experimental corrections, could resolve much of the discrepancy between the experimental data and the Lubard-Helliwell HVSL code.

Lee side total-pressure profiles at three nominal model stations are shown in Fig. 13 for a high angle-of-attack condition. As was illustrated in Fig. 12a, agreement between experiment and theory over a large portion of the viscous layer is not particularly good. For the two aft stations on the model, the pressure level in the inviscid portion of the flow field (as defined by the change in gradient of total pressure) is also poorly predicted by the Lubard-Helliwell HVSL code. The overshoot at the edge of the viscous layer is attributable to the vortex, and the reduction in the magnitude of this overshoot in moving downstream is attributable to the smaller fraction of the whole shock layer region occupied by the vortex further downstream.

The results of one lateral survey obtained by sweeping the probes across the leeward ray at a fixed location above the model centerline is shown in Fig. 14. It should be noted that this procedure resulted in the parameter y/ℓ_s also varying for each probe location. In order to obtain a comparison to the Lubard-Helliwell HVSL solution, a crossplot of numerous analytical solutions was therefore necessary. The values obtained
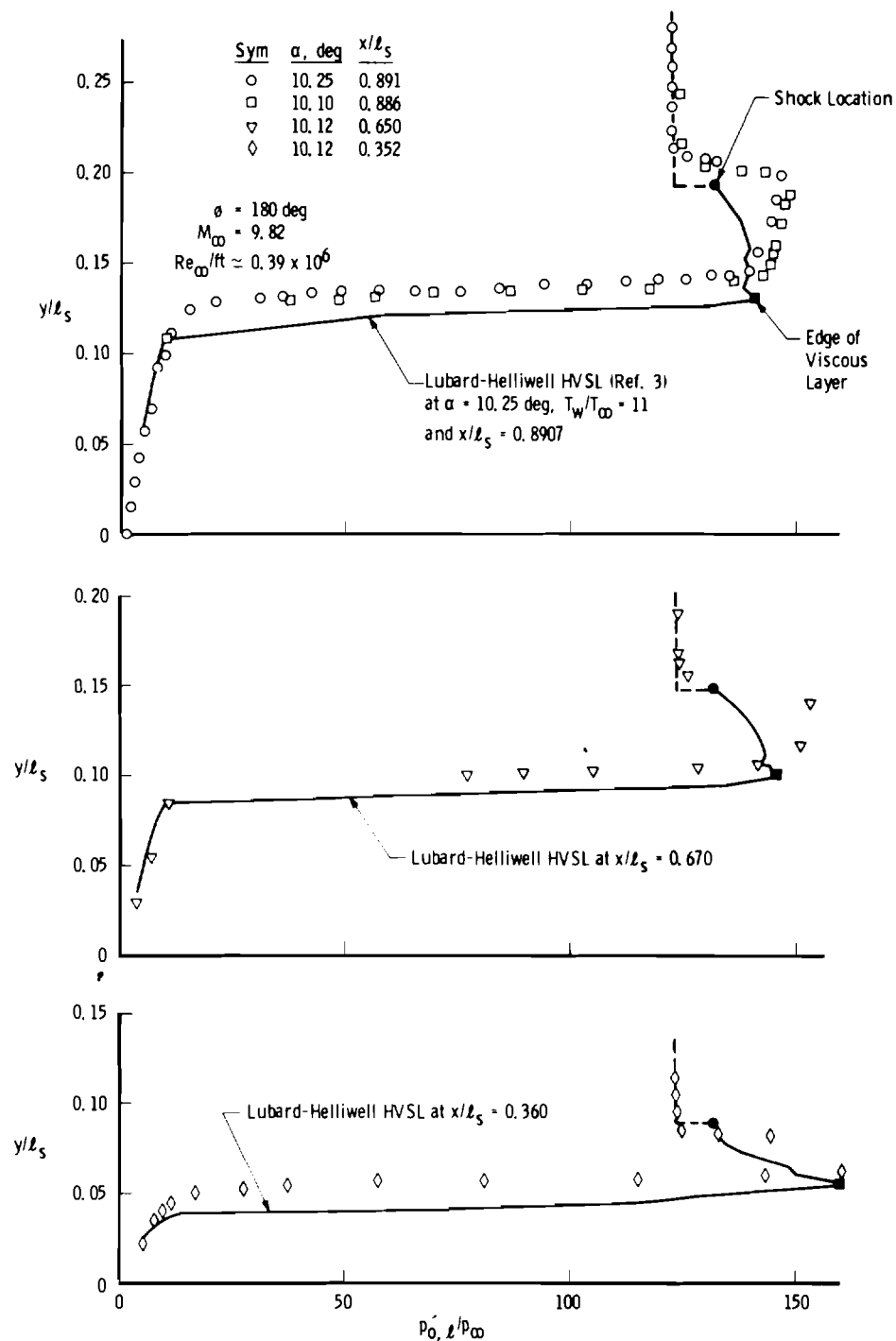
Figure 13. Boundary-layer total-pressure profiles at three stations on the lee ray of a 4-deg sharp cone at $a \cong 10.1$ deg.

from this interpolation of the analytical results are represented by the solid symbols in Fig. 14. Total pressure is slightly underpredicted, while total temperature is overpredicted for this model attitude. The measured total-temperature gradient near the shock location ($\phi \simeq 230$ deg) is not predicted by the Lubard-Helliwell HVSL code and may be attributable to the interaction of the relatively large total-temperature probe and the model shock. At least part of the difference reflected in the total-temperature data should be attributed to the perfect gas assumption employed in the analytical code.

a. **Total-pressure profile**

b. **Total-temperature profile**
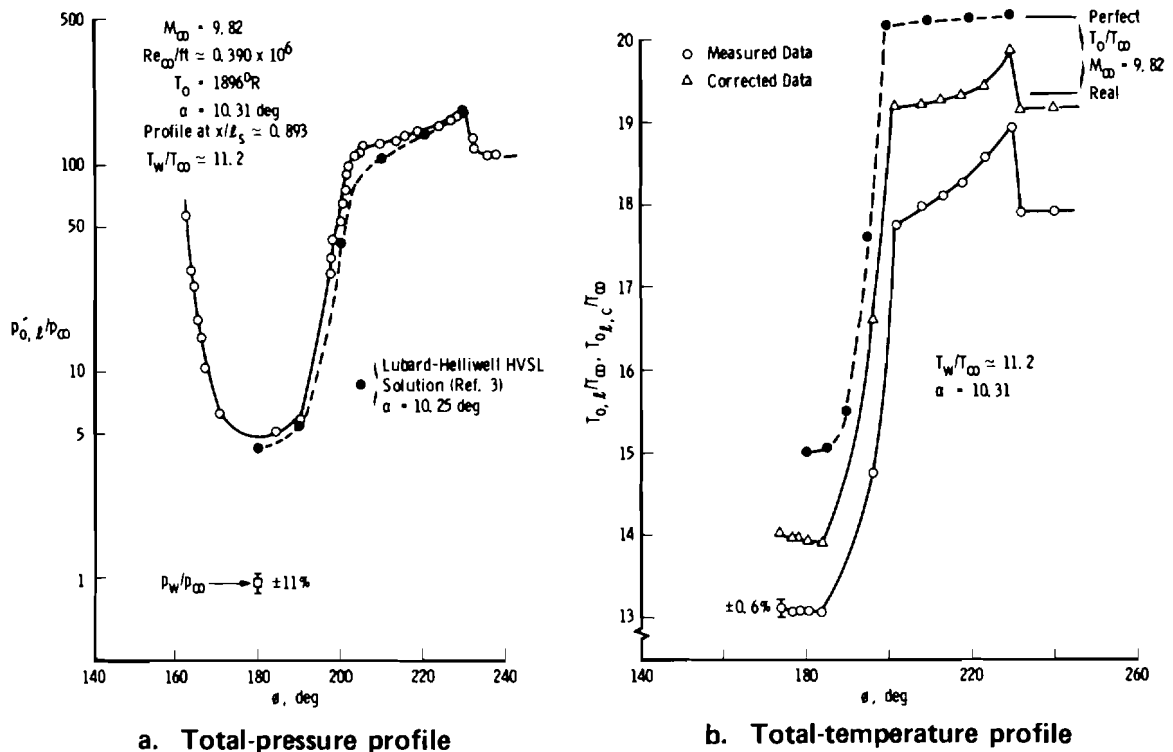
Figure 14. Lee ray flow-field lateral surveys on a 4-deg sharp cone at a = 10.31 deg.

3.6 SOURCES OF ERROR IN THE LUBARD-HELLIWELL HVSL CODE

The present comparison of the experimental data with the theoretical Lubard-Helliwell HVSL results, unfortunately, does not precisely identify the deficiencies in the theoretical solution. It is therefore imprudent at this point to list definitively the portions of the code requiring improvement. However, certain portions of the model are immediately suspect and in fact were so noted by Lubard and Helliwell in Reference 3. In the development of the code, many of the viscous terms in the Navier-Stokes equations were discarded on the basis of an order of magnitude analysis with a goal of obtaining a set of partial differential equations solvable by a streamwise marching technique. Though a potential source of theoretical error, it is precisely this set of assumptions which allows numerical solution of the problem within the speed and storage capabilities of the current

31

generation of computers. On the other hand, the consequence of the equations being made parabolic in x is that disturbances are not allowed to propagate upstream through the subsonic portion of the boundary layer; thus, the effect of the recirculating base flow is neglected. If the effect of the base region were important, the theoretical-experimental disagreement in pressure distribution should be worse nearer the base than the nose. However, Fig. 7 indicates the reverse, especially on the lee side; this probably justifies this assumption. Another set of terms was discarded from Navier-Stokes based on the assumption that the cone half-angle, or more precisely the radius measured from the cone axis ($x \sin \theta_c + y \cos \theta_c$), is not small All studies to date indicate that the Lubard-Helliwell HVSL code is fully applicable to cone half-angles of 5, 7, and 10 deg, and excellent agreement with experiment has been obtained. In contrast, the 4-deg cone represents a 20-percent reduction in cone angle from the 5-deg case, and an x/L 25 percent greater is required to reach the same radius. In conjunction with θ_c, it has been found from numerical experimentation that when the modified viscous interaction parameter $M_\infty \sqrt{\overline{Re_{\infty,\ell_s}}} \simeq 0.015$ for $\theta_c = 4$ deg, the solution becomes questionable, and at higher values the computation seems to drift off into clearly incorrect results. Theoretical stability coefficients at $M_\infty = 18$ and 25, with the same Reynolds number tested here, were found not only to exhibit large error but even showed incorrect trends. For the current solutions, $M_\infty \sqrt{\overline{Re_{\infty,\ell_s}}} \simeq 0.012$ approaches the questionable limit of 0.015. Inclusion of the discarded terms in the program would require some rather traumatic recoding. Another area to examine as a possible source of theoretical error is the temperature gradient along the model wall. The present experiment resulted in nose temperatures 20 percent hotter than the base. The original computer program contained only incomplete logic for handling this problem, and a program modification to include variable wall temperature is currently being developed. A fourth source of error is the neglect of real gas effects as previously illustrated by Figs. 12 and 13. A final source of error is the incorrect but expedient starting solution used in lieu of a precise modeling of the merged viscous-shock layer very near the nose. Inclusion of this difficult problem in the program is probably beyond the scope of the current Lubard-Helliwell HVSL code. At lower angles of attack, where the vortices are not present near the nose, Adams' starting line (Ref. 2) is an acceptable approximation for beginning the marching solution. However, at higher angles the vortex forms further and further upstream. For the case of the $a = 10$-deg, the vortex on the experimental model probably formed upstream of where the starting line was introduced in the theoretical solution ($x/\ell_s = 0.085$). Since the starting solution does not include a vortex, this may explain the improved experimental-theoretical agreement further downstream where the vortex is present in the theoretical solution.

4.0 SUMMARY AND RECOMMENDATIONS

The present data were obtained on a very slender, sharp, and slightly blunted axisymmetric cone configuration in a hypersonic, low Reynolds number flow regime which would duplicate the higher altitudes of the reentry environment. The primary purpose of the investigation was to generate experimental data to use in the development of the Lubard-Helliwell three-dimensional Hypersonic Viscous Shock Layer computer code. The present results, as compared to the existing development of the code, indicate that:

1. Surface pressures are predicted on the windward surface for a 4-deg sharp cone at incidence angles up to about 10 deg, but lee side results compare poorly as angle of attack increases (Figs. 5, 7, and 8).

2. Surface pressures on the blunt cone ($R_N/R_B = 0.225$) at an angle of attack near 3 deg are in good agreement with the Lubard-Helliwell analysis on both windward and leeward surfaces (Fig. 6).

3. The resulting sharp cone pressure-induced static aerodynamic forces and moment characteristics reflect the small differences in surface pressure levels and gradients between theory and experiment (Fig. 9).

4. Although the present flow-field measurements cannot be considered quantitative, the results suggest that the Lubard-Helliwell HVSL code predicts lee side flow-field properties on a 4-deg cone only at incidence angles less than the cone half-angle (Figs. 11 through 14). A significant portion of the discrepancy is thought to be due to formation of the vortex on the experimental model upstream of the theoretical starting solution, which does not account for the effects of the vortex.

5. The limitations of the Lubard-Helliwell HVSL code should be determined through numerical experimentation so that application beyond its valid range will not be attempted.

REFERENCES

1. Adams, J. C. and Griffith, B. J. "Hypersonic Viscous Static Stability of a Sharp 5-Deg Cone at Incidence." Article Accepted for Publication in the AIAA Journal, 1976.

2. Adams, J. C., Jr. "Numerical Calculations of the Three-Dimensional Hypersonic Viscous Shock Layer on a Sharp Cone at Incidence." Paper presented orally in the open forum session of the 2nd AIAA Computational Fluid Dynamics Conference, Hartford, Conn., June 19-20, 1975.

3. Lubard, S. C. and Helliwell, W. S. "Calculation of the Flow on a Cone at High Angle of Attack." RDA-TR-150, February 1973, R & D Associates, Santa Monica, Calif. See also AIAA Journal, Vol. 12, No. 7, July 1974, pp. 965-974.

4. Griffith, B. J., Strike, W. T., and Majors, B. M. "Ablation and Viscous Effects on the Force and Moment Characteristics of Slender Cone Models at Mach 10 Under Laminar Flow Conditions." AEDC-TR-75-109 (AD-A016396). October 1975.

5. Jones, D. J. "Numerical Solutions of the Flow Field for Conical Bodies in a Supersonic Stream." National Research Council of Canada Aeronautical Report LR-507, July 1968.

6. Marconi, F., Yaeger, L., and Hamilton, H. H. "Computation of High Speed Inviscid Flows about Real Configurations." NASA SP-347, March 1975, pp. 1411 - 1455.

7. Moretti, G. and Bleich, G. "Three-Dimensional Flow Around Blunt Bodies." AIAA Journal, Vol. 5, No. 9, September 1967, pp. 1557 - 1562.

8. Moretti, G., Grossman, B., and Marconi, F. "A Complete Numerical Technique for the Calculation of Three-Dimensional Inviscid Supersonic Flows." AIAA Paper No. 72-192, January 1972.

9. Mayne, A. W., Jr. "A Method for Computing Boundary-Layer Flows, Including Normal Pressure Gradient and Longitudinal Curvature Effects." AEDC-TR-75-21 (AD-A008739), April 1975.

10. Aungier, R. H. "A Computational Method for Exact, Direct, and Unified Solutions for Axisymmetric Flow Over Blunt Bodies of Arbitrary Shape (Program BLUNT)." AFWL-TR-70-16, July 1970.

NOMENCLATURE

A	Geometric parameter in probe coordinate system (see Fig. 4)
C_{A_p}	Axial-force coefficient due to pressure forces referenced to base area
C_{M_p}	Static pitching-moment coefficient due to pressure forces referenced to a distance x_r from the cone apex normalized by the base diameter and area
C_{N_p}	Normal-force coefficient due to pressure forces referenced to base area
C_p	Pressure coefficient, $(p_w - p_\infty)/q_\infty$
D	Model base diameter
ℓ'	Sharp cone axial length, 17.876 in.
ℓ_s	Sharp cone slant length, 17.920 in.
M_ℓ	Local Mach number at the position of the pitot probe in the cone flow field
M_∞	Free-stream Mach number
p_ℓ	Local static pressure in the cone flow field
p_o	Tunnel stilling chamber pressure
$p_{o,\ell}'$	Total pressure measured downstream of a normal shock or by a total-pressure probe in a subsonic flow field, subscript ℓ refers to local position in the cone flow field of the probe
p_w	Wall pressure
p_∞	Free-stream pressure
q_∞	Free-stream dynamic pressure
R_B	Base radius
R_N	Nose radius
Re_∞	Free-stream Reynolds number
Re_{∞,ℓ_s}	Free-stream Reynolds number based on cone slant length
r	Local body radius

T_0	Tunnel stilling chamber temperature
$T_{0,\ell}$	Local total temperature measured with the probe illustrated in Fig. 3
$T_{0\ell,c}$	Local measured total temperature corrected for internal flow viscous effects
T_w	Wall temperature
T_∞	Free-stream temperature
U_ℓ	Local velocity at the position of the total-pressure probe in the cone flow field
U_∞	Free-stream velocity
x	Coordinates in Lubard-Helliwell HVSL code (see Fig. 4)
x_r	Reference length from model nose to moment reference position
x_{cp}	Center-of-pressure location
x'	Coordinates of overhead probe traversing mechanism (see Fig. 4)
y	Coordinates in Lubard-Helliwell HVSL code (see Fig. 4)
y_s	Bow shock coordinate along a normal to model surface
y'	Coordinates of overhead probe traversing mechanism (see Fig. 4)
z'	Coordinates of overhead probe traversing mechanism (see Fig. 4)
α	Model incidence (angle of attack), deg
α_p	Overhead probe pitch setting, deg
ϵ, ϵ'	Parameters in probe coordinate system (see Fig. 4)
γ	Ratio of specific heats
ϕ	Model circumferential position, $\phi = 0$ is windward ray (see Figs. 1 and 4)
θ_c	Cone half-angle

SUBSCRIPT

i	Inviscid solutions